



# Fabrication, tuning, and high-gradient testing of an X-band traveling-wave accelerating structure for VIGAS

Xian-Cai Lin<sup>1,2</sup> · Hao Zha<sup>1,2</sup> · Jia-Ru Shi<sup>1,2</sup> · Qiang Gao<sup>1,2</sup> ·  
Jia-Yang Liu<sup>1,2</sup> · Liu-Yuan Zhou<sup>1,2</sup> · Jian Gao<sup>1,2</sup> · Huai-Bi Chen<sup>1,2</sup> ·  
Chuan-Xiang Tang<sup>1,2</sup>

Received: 9 May 2022 / Revised: 22 June 2022 / Accepted: 25 June 2022 / Published online: 20 August 2022

© The Author(s), under exclusive licence to China Science Publishing & Media Ltd. (Science Press), Shanghai Institute of Applied Physics, the Chinese Academy of Sciences, Chinese Nuclear Society 2022

**Abstract** X-band high-gradient linear accelerators are a challenging and attractive technology for compact electron linear-accelerator facilities. The Very Compact Inverse Compton Scattering Gamma-ray Source (VIGAS) program at Tsinghua University will utilize X-band high-gradient accelerating structures to boost the electron beam from 50 to 350 MeV over a short distance. A constant-impedance traveling-wave structure consisting of 72 cells working in the  $2\pi/3$  mode was designed and fabricated for this project. Precise tuning and detailed measurements were successfully applied to the structure. After 180 h of conditioning in the Tsinghua high-power test stand, the structure reached a target gradient of 80 MV/m. The breakdown rate versus gradient of this structure was measured and analyzed.

**Keywords** Traveling-wave accelerating structure · X-band high gradient · Tuning method · High-power test

## 1 Introduction

Very Compact Inverse Compton Scattering Gamma-ray Source (VIGAS) is an ongoing  $\gamma$ -ray user facility project for advanced X/ $\gamma$ -ray imaging applications at Tsinghua

University. This project employs S-band (2.856 GHz, including a photocathode electron gun, buncher, and pre-accelerating section) and X-band (11.424 GHz, main accelerating section) accelerator technology to produce low-emittance, low-energy-spread electron beams, which interact with laser pulses and generate consecutively adjustable, polarization-steerable, high-brightness and quasi-monochromatic-energy  $\gamma$ -rays with energies ranging from 0.2 to 4.8 MeV [1]. The layout of the accelerator system in the VIGAS facility is shown in Fig. 1.

In the accelerator system of the VIGAS facility, an S-band photocathode electron gun is employed to produce 5-MeV electron bunches [2]. A 1.5-m S-band traveling-wave accelerator is used to boost the energy to 50 MeV and achieve emittance compensation [3]. To reduce the energy spread caused by the longitudinal length of the bunches, a buncher is applied at the location between the photocathode electron gun and the S-band accelerator to compress the bunches to a longitudinal size. The main accelerating section of this system consists of six X-band, 0.6-m traveling-wave structures, which operate at 80 MV/m and further boost the energy to 350 MeV. The facility is operated in single-bunch mode, and the electron bunch is accelerated at the maximum voltage point determined by the pulse after the pulse compressor. The output energy of the system is adjusted by altering the accelerating gradient and phase of the X-band accelerators.

An X-band high-gradient accelerator plays a key role in decreasing the volume of the entire system in VIGAS. This technology can be traced back to electron–positron Global Linear Collider (GLC) [4, 5] and Next Linear Collider (NLC) [6, 7] studies for which the SLAC National Accelerator Laboratory and High Energy Accelerator Research Organization (KEK) collaborated in the late

This work was supported by the National Natural Science Foundation of China (Nos. 11922504 and 12027902).

✉ Jia-Ru Shi  
shij@mail.tsinghua.edu.cn

<sup>1</sup> Department of Engineering Physics, Tsinghua University, Beijing 100084, China

<sup>2</sup> Key Laboratory of Particle and Radiation Imaging (Tsinghua University), Ministry of Education, Beijing 100084, China

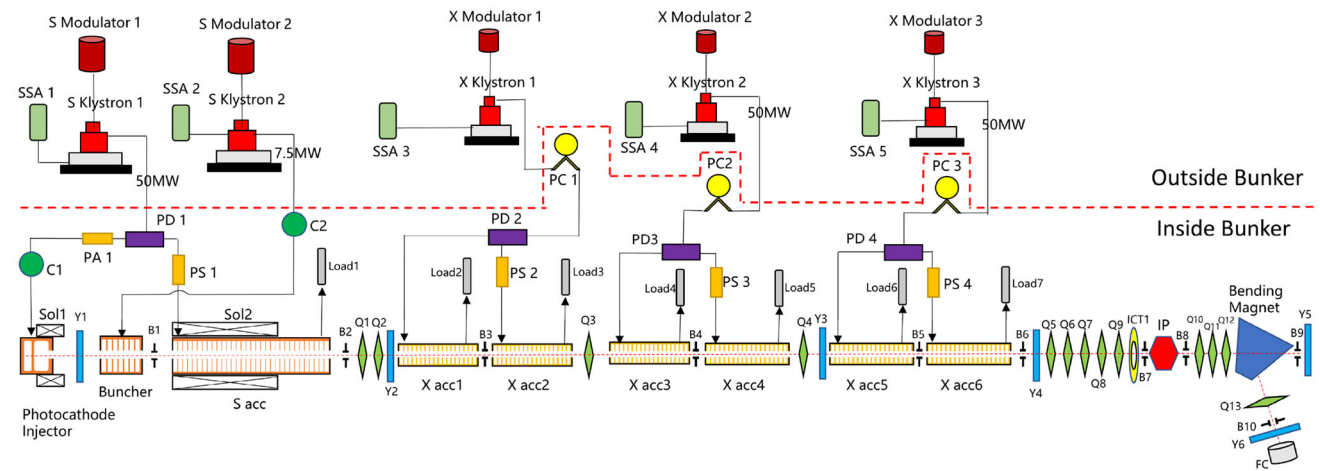


**Fig. 1** (Color online) Layout of the accelerator system of the Very Compact Inverse Compton Scattering Gamma-ray Source (VIGAS) facility. Abbreviations in this figure are defined as follows: PC: pulse compressor; PD: power divider; PA/PS: power attenuator/phase

shifter; C: circulators; acc: accelerator; sol: solenoid; Y: YAG screen; B: beam position monitor; Q: quadrupole; ICT: integrated current transformer; IP: interaction point; FC: Faraday cup

1980s. A high gradient of 65 MV/m was reported at the Next Linear Collider Test Accelerator (NLCTA) by SLAC [8] and the new X-band test facility (XTF) by KEK [9] prior to 2005. The Compact Linear Collider (CLIC) program at the European Organization for Nuclear Research (CERN) changed the frequency from 30 to 12 GHz based on the experimental results in 2007 and obtained a gradient of 100 MV/m [10] in an initial X-band structure test.

In addition to the large colliders, X-band high-gradient technology is also applied to the design of free-electron laser (FEL) facilities, such as a soft X-ray FEL known as ZFEL at the University of Groningen [11] and a hard X-ray FEL using an all-X-band accelerator at SLAC [12]. In 2017, an X-band accelerating structure for a compact hard X-ray FEL facility was designed at the Shanghai Institute of Applied Physics [13]. In recent years, there has been a growing interest in utilizing high-gradient technology in compact inverse Compton scattering sources, such as VIGAS and Smart\*Light at the Delft University of Technology [14].

Tsinghua University collaborated with CERN and KEK to assess the feasibility of X-band high-gradient accelerating structures and now has the capacity to machine, rinse, and braze X-band high-gradient structures. A choke-mode high-gradient structure was designed by Tsinghua University, which reached a gradient of 120 MV/m [15]. An X-band high-power test stand, where high-gradient structures can be tested, was established at Tsinghua University. An X-band high-gradient two-half structure [16] and a field-emission gun [17] were designed and tested in this high-power test stand.

Accelerating structures can be divided into traveling-wave and standing-wave structures. Owing to the wide-

pass band property, the traveling-wave structure can be operated without a circulator and is more favorable for long high-gradient structures. Traveling-wave structures include constant-impedance (CI) and constant-gradient (CG) structures. A CI structure is formed using identical cells. Owing to wall loss, the gradient at the rear of the structure is lower than that at the front. In contrast, for a CG structure, a gradually decreasing group velocity is adopted to generate a uniform field distribution. Nevertheless, the tested high-gradient structure adopted a CI scheme, whose fabrication is more reliable and less costly. A high-power test is important for the application of X-band high-gradient technology.

In this paper, the design of a CI high-gradient structure with a SLED-I type radio-frequency (RF) pulse compressor (PC) is reviewed, and the fabrication process of this structure is introduced. The application of a non-contact tuning method to this structure and the RF measurements after tuning are shown. A high-gradient test is demonstrated, including the conditioning history, the highest achieved gradient, and the spatial distribution of breakdown inside the structure. The breakdown rate (BDR) versus the gradient of this structure was measured to analyze its high-gradient performance.

## 2 Design and fabrication of the CI structure

The X-band high-gradient structure in VIGAS will be operated with a SLED-I type PC. The calculation of the accelerating gradient and the design of the structure are shown in Ref. [18]. The reason for selecting a CI scheme instead of a CG scheme is explained as follows.

The accelerating gradient in each cell for both schemes with and without a PC is shown in Fig. 2. The filling time of the CG structure was set at the same value as that of the CI structure. Both were assumed to operate with the same PC. To maintain the highest accelerating voltage, electrons should exit the structure when the filling of this structure is completed [19]. Considering that the filling time of the structure ( $\sim 100$  ns) is significantly longer than the time that an electron spends traveling through the structure ( $\sim 2$  ns), electrons should be injected into the structure when the filling of the entire structure is almost complete. Consequently, for a CG structure, an electron travels through a higher accelerating field in the rear part than at the front. In contrast, the declining nature of the power flow along the beam path of a CI structure can compensate for the effect of the declining output of the PC. As a result, when transforming from the scenario without a PC to that with a PC, the accelerating voltage gain of the CI structure is slightly higher than that of the CG structure. Integration of the gradients of cells in Fig. 2 showed that the ratio of accelerating voltage with and without a PC was 2.17 and 2.15 for the CI and CG structures, respectively. Consequently, the accelerating voltage of the CI structure with a PC was 0.1% higher than that of the CG structure, whereas for the case without a PC, the former was 0.5% less than the latter. Therefore, when operating with a PC, a CI structure is more favorable than a CG structure in terms of the accelerating voltage. Furthermore, owing to the identical dimensions of all normal cells, the elaborate fabrication of the structure is more reliable, and the cost of fabricating a CI structure is estimated to be over 20% less than that of a CG structure, which has great significance for

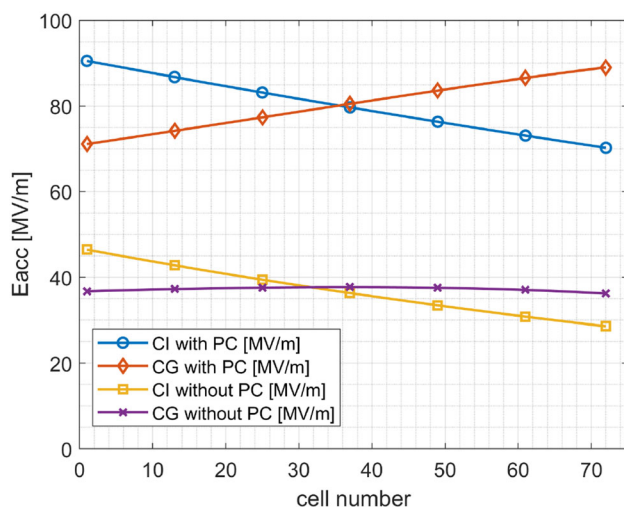


**Fig. 2** (Color online) Comparison of the accelerating gradient in each cell for the CI and CG structures with and without a PC. The input power is 13.7 MW. The input signal for the PC has ideal phase switching (phase switching time is zero). The CI and CG structures used for the calculation have equal filling times

the industrial application of X-band high-gradient technology.

The shape of a periodic cell is shown in Fig. 3a. Optimization of a single cell, including the maximum surface electric field and modified Poynting vector, was achieved and introduced in Ref. [18]. A dual-feed scheme was adopted for the coupler, as shown in Fig. 3b. An 8-mm rounding was designed at the juncture of the matching cell and coupling hole to reduce the local magnetic field enhancement. Compared to the 2-mm scheme, the maximum magnetic field was reduced by 17%. The surface electric and magnetic fields of the input coupler and its adjacent cells are shown in Fig. 3c and d. The optimization process of the coupler is introduced in Ref. [20].

A photograph of a machined cavity is shown in Fig. 4a. Two holes were formed to insert a tuner. The coupler consisted of two parts that were processed by the milling machine. These two parts were brazed and reprocessed to match the WR90 waveguide. A photograph of the coupler after reprocessing is shown in Fig. 4b. After fine machining with an accuracy of 10  $\mu\text{m}$  and a surface roughness of 25 nm, cavities were measured using non-contact field measurement to determine their frequency in the working mode [21]. Compared with measurements utilizing a detuning plunger, this method has a significantly lower probability of damaging the iris of the cavity, where breakdown is more likely to occur for a high-gradient structure. The cavities were brazed as a cell stack before being brazed with the coupler and flange. The entire structure was brazed with a gold–copper solder. Compared with silver–copper solders, gold–copper solders reduce dark current according to the Fowler–Nordheim equation [22] because the work function of gold is higher than that of silver.

### 3 RF measurement and tuning method

After fabrication, tuning and RF measurements were performed on the structure. A traveling-wave structure is usually designed to work with a reflection below  $-30$  dB from the input coupler and correct the phase shift between cells along the beam path to accelerate the charged particle. The phase shift between adjacent cells is of critical importance because it directly influences the accelerating performance. However, the mechanical tolerance of the cell diameter during fabrication is approximately 10  $\mu\text{m}$ , which causes a frequency shift of approximately 5 MHz and a  $5^\circ$  cell-to-cell phase advance shift in an X-band structure [23]. This means that the structure must be tuned after fabrication to compensate for the mechanical errors.

A non-contact tuning method requires the measurement of field distribution, which is measured using the non-

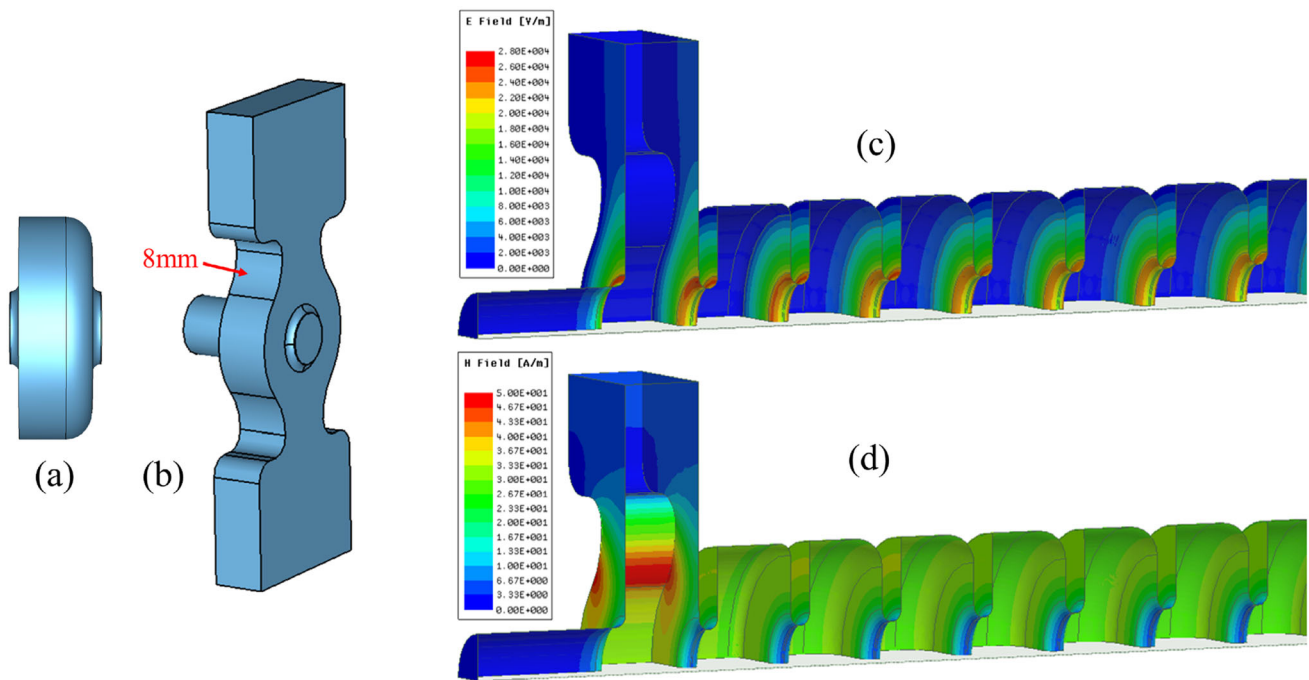
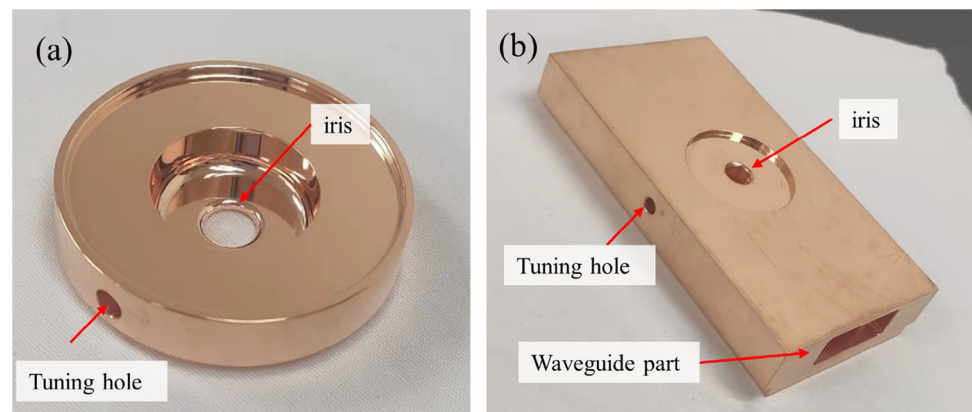


**Fig. 3** (Color online) **a** Three-dimensional (3D) model of the periodic cell; **b** 3D model of the coupler; **c** Surface electric field of the input coupler and its adjacent cells; **d** Surface magnetic field of the input coupler and its adjacent cells

**Fig. 4** (Color online) **a** Photograph of a cavity after fine machining and **b** photograph of a coupler after fine machining, brazed, and reprocessed



resonant method, also known as the bead-pull method. According to Ref. [24],

$$2P_i(S_{11,p} - S_{11,a}) = -j\omega k E_a^2 \quad (1)$$

where  $P_i$  is the input power,  $S_{11,p}$  is the reflection coefficient in the presence of a perturbing object,  $S_{11,a}$  is the reflection coefficient in the absence of a perturbing object,  $k$  is a coefficient that depends on the electric parameters and geometry of the object, and  $E_a$  is the complex electric field. Generally, only the relative electric field is considered in RF measurements. The electric field is proportional to the difference between the reflection coefficient in the presence and absence of a perturbing object.

In this experiment, a 0.14-mm nylon thread with a  $\phi$  0.14 mm  $\times$  0.7 mm metal bead was inserted through the

structure and laid on its axis. When the metal bead passed through each cell, the vector network analyzer (VNA) measured and recorded the change in reflection, including its magnitude and phase. Using Eq. (1), the relative electric field magnitude and phase of each cell were obtained.

The setup for RF measurements is shown in Fig. 5. The structure was laid horizontally instead of vertically because this layout was more convenient for tuning. To avoid the installation of a power divider and bend waveguides, two ports of the VNA were connected to the input coupler. The VNA could transform the  $S$ -parameter from these two ports into a combined reflection. This method is introduced in Ref. [25]. Because one port of the VNA malfunctioned when performing the measurement, two matched loads were assembled at the output coupler instead of the

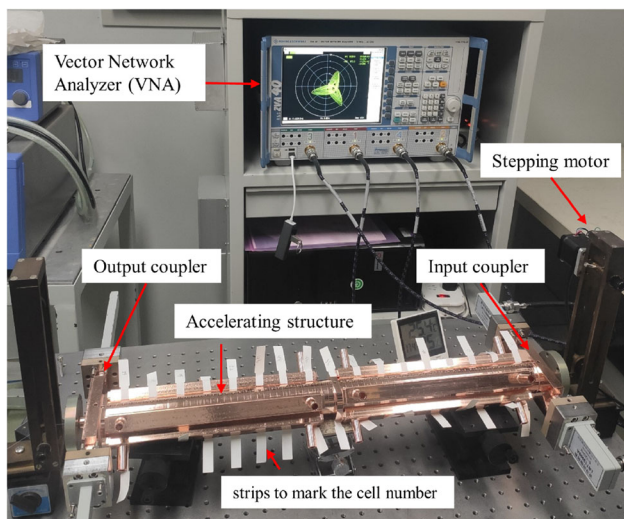


**Fig. 5** (Color online) Photograph of the RF measurement of the traveling-wave structure

remaining two ports of the VNA. The full  $S$ -parameters of this structure were measured by changing the connection location of the ports between the VNA and the structure.

The frequency shift of each cell was derived from the measured field distribution using the method introduced in Ref. [23]. The local reflection of the  $n$ -th cell can be calculated using Eq. (2).

$$\Gamma_{11}^{\text{local}} = \frac{2E_n \cos \varphi - (E_{n-1} + E_{n+1})}{E_{n-1} - E_n e^{-j\varphi}} \quad (2)$$

where  $E_n$  is the measured complex field of the  $n$ -th cell, counted by the input coupler. In general, the maximum field value in the beam path of a cell is used.  $E_{n-1}$  and  $E_{n+1}$  are the values in the adjacent cells, and  $\varphi$  is the designed phase advance, that is, the working mode of the structure. The relationship between the local reflection and the frequency shift is shown in Eq. (3).

$$\Delta f_n = \frac{\varphi \text{Imag}\{\Gamma_{11}^{\text{local}}\}}{f_0 v_g/c} \quad (3)$$

where  $\varphi$  is the working mode,  $f_0$  is the resonance frequency of the cavity,  $v_g$  is the group velocity, and  $c$  is the speed of light. In the non-contact tuning situation, the reflection from the input port (global reflection) was monitored to guide the tuning of each cell. Because the frequency change of the  $n$ -th cell could not be obtained directly from the global reflection, the tuning strategy was to compensate for its local reflection. The variation in reflection from the input port is the local reflection multiplied by the round-trip transmission loss between the input coupler and the  $n$ -th cell [23]. Tuning of the middle cells is achieved when the local reflection of each cell is compensated.

Owing to fabrication errors in the output coupler, such as machining tolerance and solder leakage into the cavity during brazing, the output matching cell and its adjacent cell should be tuned to minimize the reflection from the output coupler to the middle cells [23]. The input coupler was tuned to minimize global reflection. During the tuning procedure, field measurements were performed at the working frequency. A temperature of 25.4 °C and a humidity of 25% were used to calculate the frequency amendment between the environment during RF measurement and operation, as described in Ref. [26]. The field distribution before and after tuning is shown in Fig. 6.

The phase advance between the adjacent cells before and after tuning is shown in Fig. 7. Before tuning, the phase advance between adjacent cells varied from 60° to 150°, with a mean angle of 119.5°. During the tuning process, each phase advance between adjacent cells was tuned to 120°, that is, the  $2\pi/3$  working mode. After tuning, the phase advance was next to the working mode, with a maximum deviation of 5°. The comparison in Fig. 7 reveals the favorable effects of tuning.

The  $S$ -parameters after tuning were measured and are shown in Fig. 8. The reflection from the input coupler was below -30 dB, whereas the reflection from the output coupler was only -12 dB. This indicates that the reflection is relatively large when power is fed from the output coupler. Although the CI structure is symmetric in the design phase, which means that power can be fed from either the input or output port, it is necessary to distinguish the two ports after tuning. The transmission loss measured in this experiment was -6.5 dB.

The filling time was obtained using the  $S_{12}$  parameter. For a periodic structure, the transmission coefficients can be derived from the circuit model [27, 28] and expressed as Eq. (4).

$$S_{12} = e^{-\alpha n D} e^{-j(n\varphi + \varphi_0)} \quad (4)$$

where  $\alpha$  is the attenuation factor,  $n$  is the cell number,  $D$  is the length of one cell,  $\varphi$  is the phase advance of adjacent cells, and  $\varphi_0$  is the phase introduced by the waveguides and other components. Both  $\alpha$  and  $\varphi$  are functions of frequency. According to this definition, the group velocity  $v_g = d\omega/d\beta$ . When the structure operates at the designed frequency, its phase velocity equals the speed of light, that is,  $v_p = \omega_0/\beta = c$ . The relationship between the phase advance and cell length is  $D = \varphi c/\omega_0 = \varphi/\beta$ . By combining these equations, the filling time at the working frequency can be derived using Eq. (5).

$$t_f = \frac{nD}{v_g} = nD \frac{d\beta}{d\omega} \Big|_{\omega_0} = n \frac{d\varphi}{d\omega} \Big|_{\omega_0} = - \frac{d(\text{Angle}\{S_{12}\})}{d\omega} \Big|_{\omega_0}, \quad (5)$$

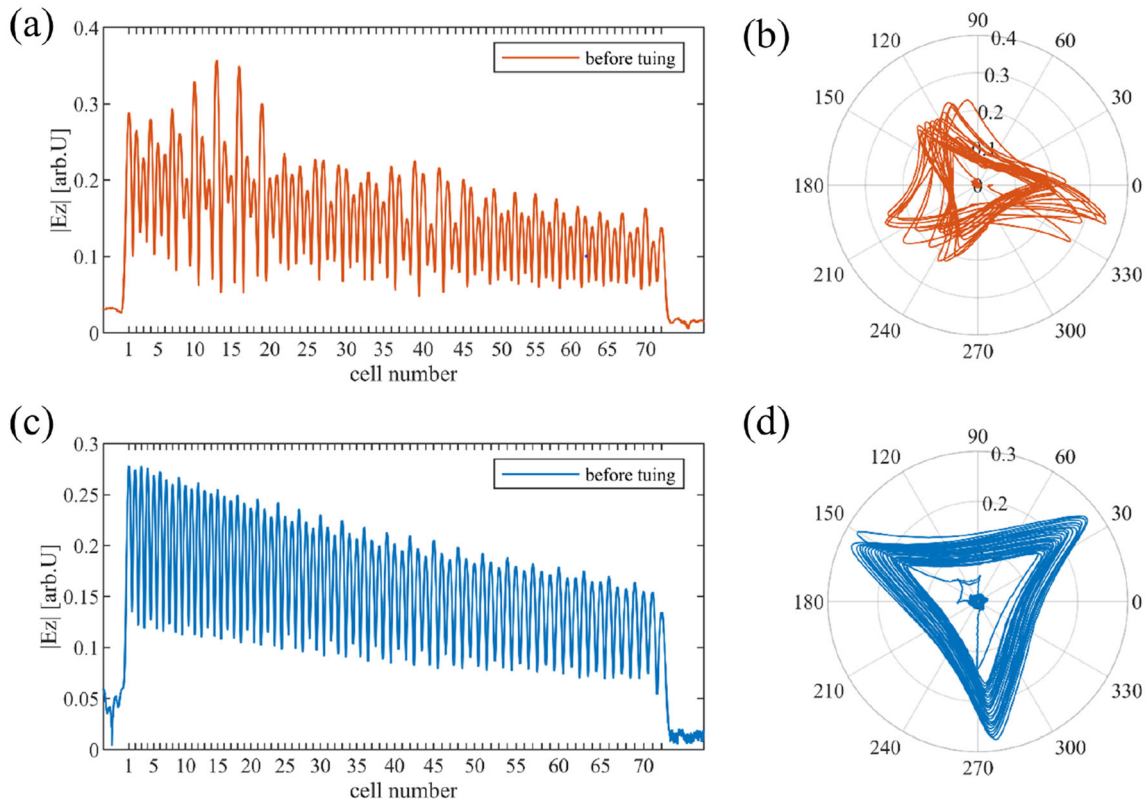
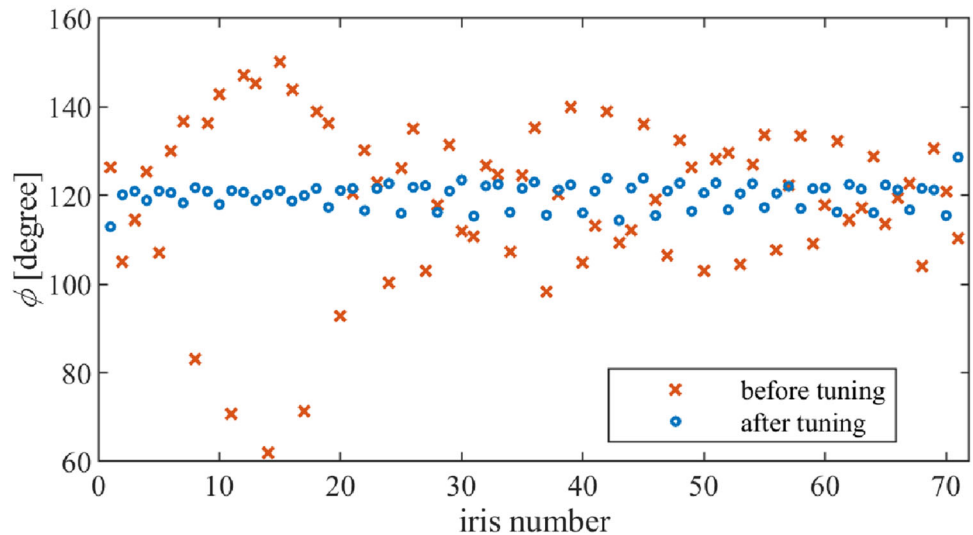


**Fig. 6** (Color online) RF measurement results of the traveling-wave structure before and after tuning. **a** Relative magnitude of the electric field before tuning; **b** Polar plot of the complex electric field before

tuning; **c** Relative magnitude of the electric field after tuning; **d** Polar plot of the complex electric field after tuning;

**Fig. 7** Phase advance between adjacent cells before and after tuning



The filling time calculated using Eq. (5) was 98 ns. The group velocity obtained from this measured filling time was 2.14%  $c$ , which is close to the designed value of 2.2%  $c$ . For the CI structure, the  $Q$  value was calculated from the attenuator factor using Eq. (6).

$$Q = \frac{\omega}{2\alpha v_g} \tag{6}$$

According to Eq. (4),  $\alpha$  can be obtained from the magnitude of the  $S_{21}$  parameter. Another method of measuring the attenuation factor for a CI structure is to perform an

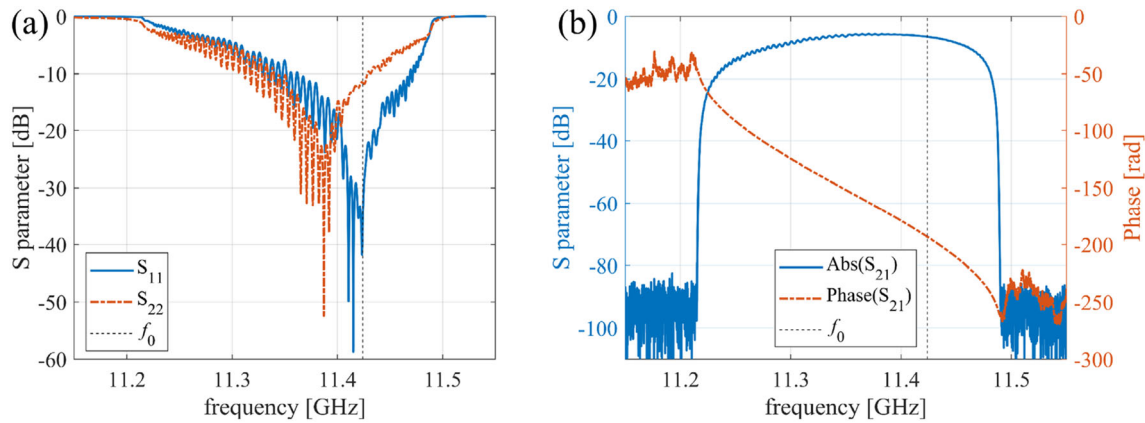


**Fig. 8** (Color online) *S*-parameters of the structure after tuning. **a** Magnitude of *S*<sub>11</sub> and *S*<sub>22</sub> in dB and **b** magnitude and unwrapped phase of *S*<sub>21</sub>. The black dashed line is the location of the working frequency at  $2\pi/3$

exponential fit of the tuned field distribution. In this RF measurement, the *Q* values measured from the *S*<sub>21</sub> parameter and field distribution were  $4.7 \times 10^3$  and  $5.7 \times 10^3$ , respectively. The former was 18% lower than the latter, whereas the latter was closer to the designed value of  $7.0 \times 10^3$ . Considering that there may be a calibration error or other transmission losses in the measurement, the second value was adopted as the measured *Q* value. A comparison of the RF measurement results before and after tuning, as well as the simulation results, are reported in Table 1.

#### 4 High-gradient testing and analyses

The high-gradient traveling-wave structure was tested using the Tsinghua X-band high-power test stand (TpoT-X). The TpoT-X was powered by a 40 Hz, 50 MW klystron, and a series of X-band high-power and high-gradient experiments were conducted. A system diagram of the TpoT-X is presented in Ref. [16]. The TpoT-X was split into a power source room, in which the klystron, its modulator, and front signal source were placed, and a shielded room, where the devices under testing were installed. In 2019, an adjustable power divider was installed in the shielded room to increase the testing capacity of the platform [29]. A photograph of the structure after the

installation is shown in Fig. 9. The high microwave power of the klystron was enhanced using a corrugated PC. After compression, power was fed into the structure via a power splitter and two 180° H-bends. The transmitted power from the output coupler was absorbed by an X-band stainless steel RF load scaled from the S-band load [30]. Directional couplers were placed in front of the input coupler and behind the output coupler. A Faraday cup was installed at the downstream port of the structure to capture the dark current. During the high-power test, the input, output, and reflected signals were measured by an oscilloscope via a directional coupler, coaxial attenuator, and crystal detector.

An automated conditioning system was used for the TpoT-X. Waveforms from the oscilloscope were recorded at regular time intervals. If the magnitude of a reflected wave is detected to be five times larger than that of the normal wave, the system would consider this a breakdown event and pause for a set time; the supplied power would also be lowered when restarting the power source.

Two sets of representative waveforms from normal and breakdown scenarios were selected from the recorded data saved by the automated conditioning system, as shown in Fig. 10. The input pulse to the structure, that is, the output pulse from the PC, had a declining pulse top owing to the energy-releasing process of the PC. Figure 10 shows only the waveform after phase inversion. The entire waveform from the PC is shown in Ref. [31]. In the normal case, the

**Table 1** Comparison of RF measurement results and simulation results

Parameter	Before tuning	After tuning	Simulation value
Average phase advance (°)	119.5	120.0	120.0
Standard deviation of phase advance (°)	17.6	2.9	0.4
Reflection (dB)	- 21	- 34	- 50
Filling time (ns)		98	94
Group velocity/ <i>c</i>		2.14%	2.2%
Quality factor		$5.7 \times 10^3$	$7.0 \times 10^3$

**Fig. 9** (Color online) Photograph of the structure after installation in the Tsinghua X-band high-power test stand

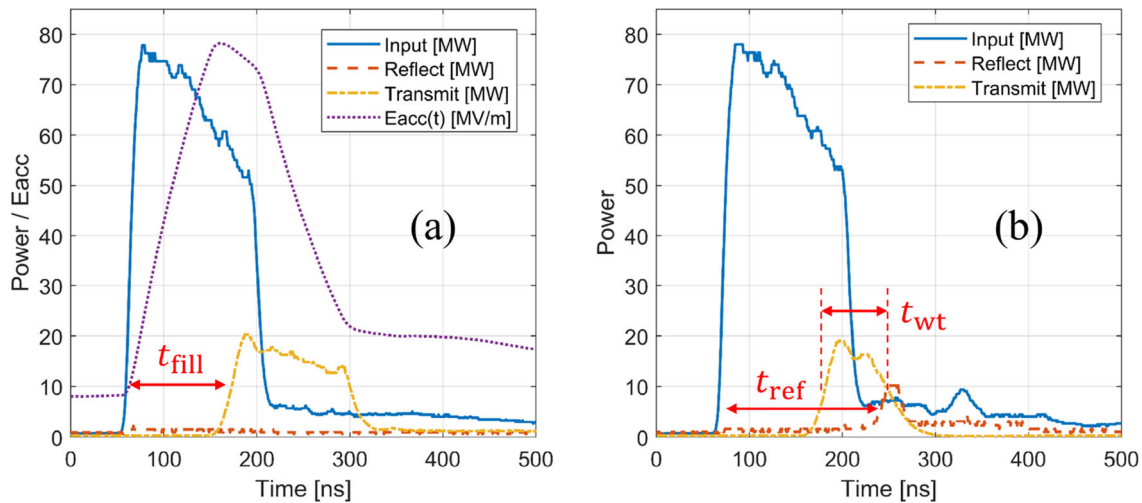
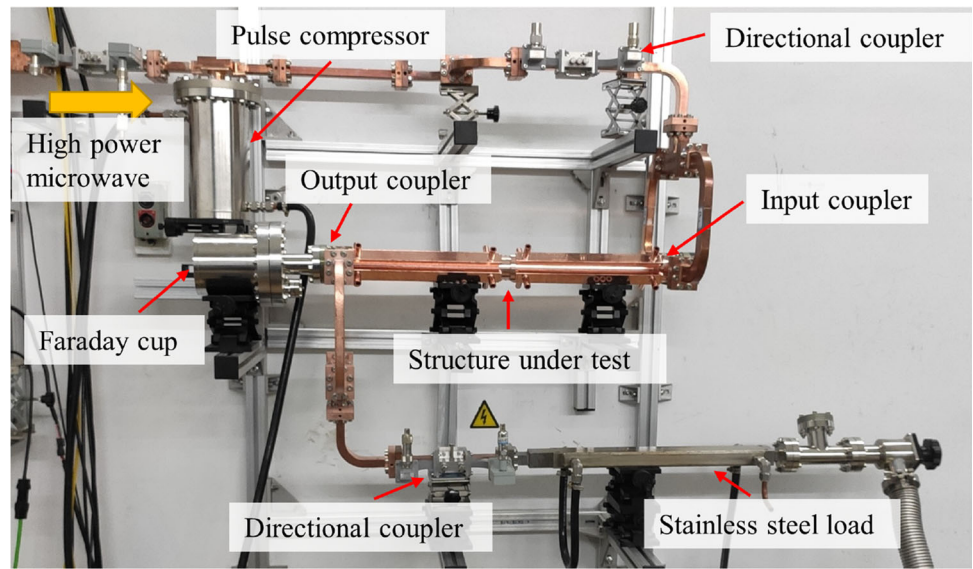


**Fig. 10** (Color online) Waveforms and accelerating gradient in the normal and breakdown cases of the conditioning process. **a** Input (blue solid line), reflected (red dash line), and transmitted (yellow dot-dash line) waveforms of the structure and accelerating gradient versus injection time (purple dotted line) in the normal case. The accelerating gradient versus injection time is calculated using Eq. 7. **b** Input

(blue solid line), reflected (red dash line), and transmitted (yellow dot-dash line) waveforms of the structure in the breakdown case. Inside the figure,  $t_{fill}$  is the filling time of the structure,  $t_{ref}$  is the time between the rising edges of the input and reflected signals, and  $t_{wt}$  is the pulse width of the transmitted pulse

transmitted wave occurred approximately 100 ns after the input pulse. This value represents the filling time of the entire structure. Because of the broadband properties of the long traveling structure, the output wave was not obviously broadened compared with the input wave. The accelerating gradient versus injection time in Fig. 10a was calculated using Eq. (7).

$$E_{acc}(t) = \frac{1}{L} \int_0^L \sqrt{\frac{\omega r}{v_g Q}} P\left(t - \frac{z}{c}\right) e^{-\alpha z} dz \tag{7}$$

where  $L$  is the length of the structure,  $\omega$  is the working frequency,  $v_g$  is the group velocity,  $r$  is the shunt

impedance per meter,  $Q$  is the intrinsic quality factor,  $P$  is the input power waveform,  $t$  is the injection time of the electron beam to the structure,  $c$  is the speed of light, and  $\alpha$  is the attenuation factor. In the breakdown case, because of the blocking effect of the plasmid generated at the breakdown location, the transmitted wave was shortened, and the magnitude of the reflected wave was remarkably larger than that in the normal case. The time marked in Fig. 10b was used to calculate the breakdown location inside the structure.

After 180 h of conditioning, this structure had undergone  $1.75 \times 10^7$  pulses and reached the designed gradient



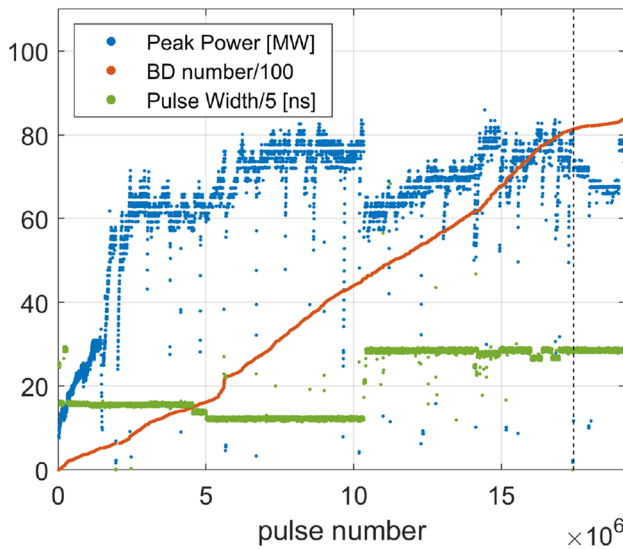


**Fig. 11** (Color online) Conditioning history and testing of the high-gradient structure. The black dashed line is the dividing line of conditioning and testing

of 80 MV/m. The conditioning history is shown in Fig. 11. The maximum input power was 83 MW, and the overall breakdown number was  $8.4 \times 10^3$ . During the conditioning process, 78-ns pulses were employed. Because of the slow growth rate, the pulse width was reduced to 60 ns. From  $5 \times 10^6$  to  $10.3 \times 10^6$  pulses, the input peak power was improved at a faster pace. When the expected input power was reached, the input pulse width was increased to the required value of 143 ns, and the input power was again increased to 83 MW. After conditioning, this structure was tested at three fixed gradient levels with a 143-ns input pulse, and the BDR was measured at these levels.

The maximum gradient of the first cell of the structure during the filling procedure was calculated directly using the input peak power and shunt impedance as approximately 110 MV/m. This is comparable to existing high-gradient records. The average accelerating gradient of the entire structure can be expressed as  $E_{acc} = \max\{E_{acc}(t)\}$ , for which  $E_{acc}(t)$  is calculated using Eq. (7). The average accelerating gradient during the conditioning process is shown in Fig. 12. The gradient exhibited a leap at a pulse number of  $10.2 \times 10^6$  because the structure converted from a partially filled status to fully filled status owing to the increase in the input pulse. The maximum surface electric field and modified Poynting vector were calculated from the input peak power and simulation field data. Figure 12 b and d shows that the maximum surface electric field was 225 MV/m, and the maximum modified Poynting vector was  $5.5 \text{ MW/mm}^2$ . Pulse heating was calculated using the maximum surface magnetic field and input pulse form, as introduced in Ref. [32]. Pulse heating during the conditioning process is shown in Fig. 12c.

The breakdown location is obtained from the input, transmitted, and reflected signals by this physics image [33]: when the input pulse is transmitting through the structure, part of the pulse is blocked at the breakdown location and reflected back to the input coupler as a reflected signal, and the remaining part is transmitted to the output coupler as a transmitted signal. The pulse width of the transmitted signal  $t_{wt}$  represents the breakdown time inside the input pulse. The retardation time of the reflected signal  $t_{ref}$  represents the round-trip time of the signal between the input coupler and the breakdown site. Therefore, the distance from the input coupler to the breakdown site can be calculated using Eq. (8).

$$L_{BD} = v_g \cdot (t_{ref} - t_{wt})/2 \tag{8}$$

A sketch map of  $t_{ref}$  and  $t_{wt}$  is shown in Fig. 10, and the spatial breakdown distribution is shown in Fig. 13. Owing to the complex circumstances in which breakdown occurs, the transmitted and reflected signals may have an irregular shape, which leads to difficulties in confirming  $t_{ref}$  and  $t_{wt}$ . Therefore, the breakdown location calculated using this method may have an error range of several cells. Nevertheless, the distribution trend still conveyed information. As expected, breakdown was more likely to occur at the input side of the structure, where the surface electric field and modified Poynting vector were higher. At the rear part of the structure, very few breakdowns occurred.

During the testing period, the relationship between the measured BDR and gradient was measured, as shown in Fig. 14. The linear fitting coefficient of the data in the double logarithmic plot was  $23.8 \pm 6.7$ , which is analogous to an empirical value of 30. The error value was large because of the limited range of gradients that could be tested. According to the fitting curve, this structure could be operated at 80 MV/m with a BDR level of approximately  $1.1 \times 10^{-3} /(\text{pulse}\cdot\text{m})$ . This rate is expected to decrease by a level of one to two orders when the conditioning pulse increases  $10^8$  [15]. Because of the other assignments on this platform, further conditioning was not performed.

### 5 Conclusion

In this study, the RF measurement, tuning, and high-gradient testing of a CI high-gradient structure were demonstrated. Compared to a CG structure, the fabrication of a CI structure has a lower cost and is more reliable, and the accelerating voltage is slightly higher with a PC. This makes the CI structure more suitable for applications if the target gradient is reached. After 180 h of conditioning, this CI structure had undergone  $1.75 \times 10^7$  pulses and reached the designed gradient of 80 MV/m. The breakdown location

**Fig. 12** (Color online) Accelerating gradient and surface parameters in the conditioning process. **a** Accelerating gradient calculated by integrating the input waveform; **b** maximum surface electric field; **c** maximum pulse heating; and **d** maximum modified Poynting vector

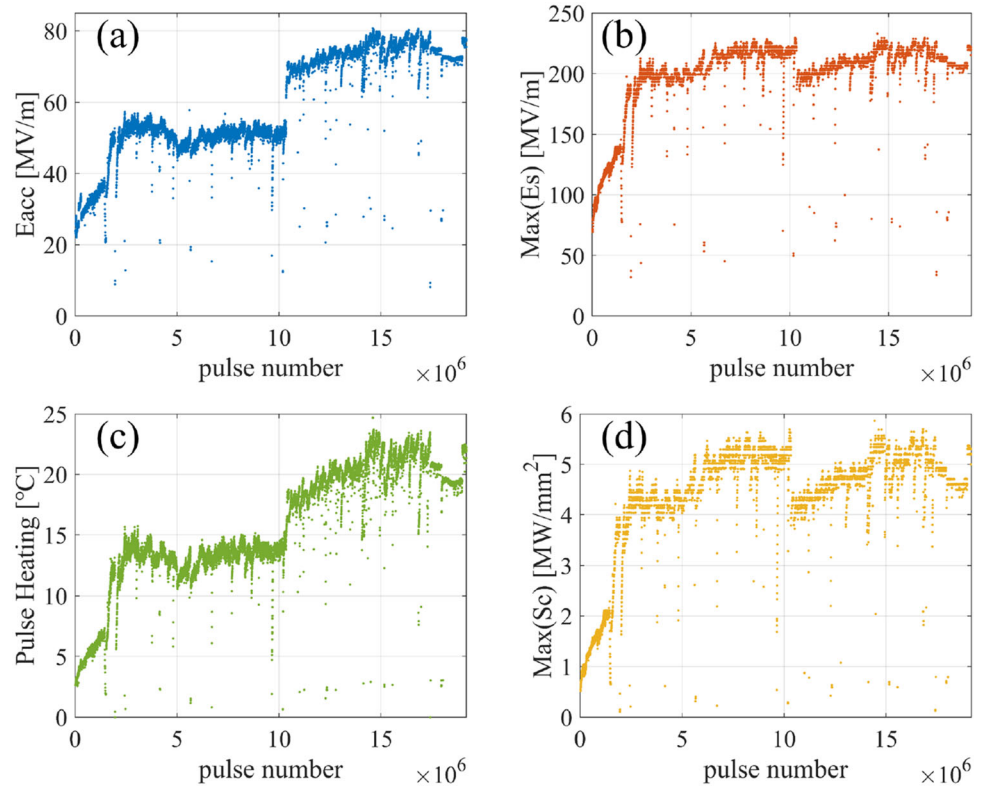
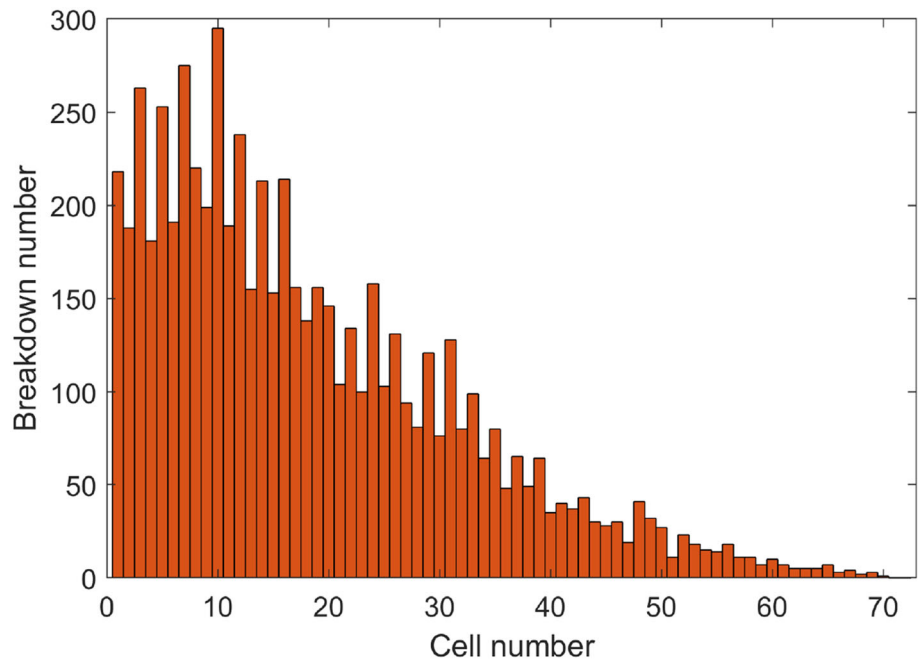


**Fig. 13** (Color online) Distribution of the structure's breakdown location



analysis showed that breakdown was concentrated at the front part of the structure, where the surface field was higher. Extrapolation from the measured BDR showed that this structure could be operated at 70 MV/m with a BDR of approximately  $4.4 \times 10^{-5}/(\text{pulse m})$ . The application of this

structure at this gradient level was verified. To utilize this structure with a gradient of 80 MV/m at VIGAS and a BDR of  $10^{-5}/(\text{pulse m})$ , further conditioning pulses are required. Furthermore, a CG scheme has a lower surface field, and therefore fewer conditioning pulses are required to reach the

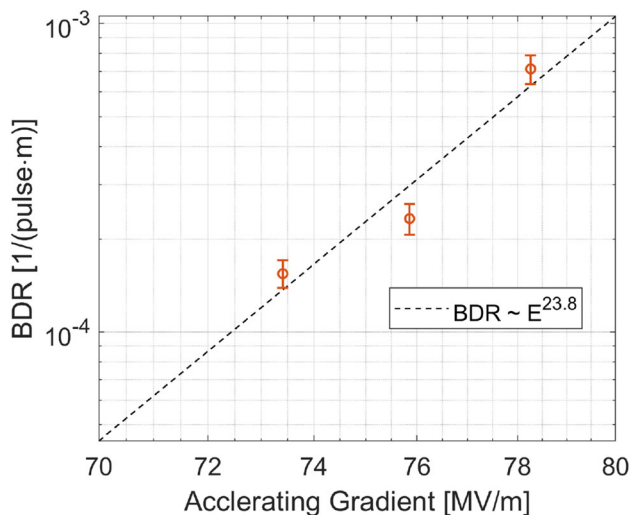


**Fig. 14** Measured BDR versus accelerating gradient

same gradient compared with a CI scheme according to the experimental results. This is also considered for the VIGAS program.

**Author contributions** All the authors contributed to the conception and design of the study. Material preparation, data collection, and analysis were performed by Xian-Cai Lin, Liu-Yuan Zhou, Qiang Gao, Jian Gao, and Jia-Yang Liu. The first draft of the manuscript was written by Xian-Cai Lin, and all the authors commented on the previous versions of the manuscript. All authors have read and approved the final manuscript.

## References

- H. Chen, Y. Du, L. Yan et al., Optimization of the compact gamma-ray source based on inverse Compton scattering design. 2018 IEEE Advanced Accelerator Concepts Workshop (AAC), 1–5 (2018). <https://doi.org/10.1109/AAC.2018.8659417>
- L. Zheng, Y. Du, Z. Zhang et al., Development of S-band photocathode RF guns at Tsinghua University. Nucl. Instrum. Methods Phys. Res. Sect. A. **834**, 98–107 (2016). <https://doi.org/10.1016/j.nima.2016.07.015>
- D. Cao, J. Shi, H. Zha et al., Electromagnetic and mechanical design of high gradient S-band accelerator in TTX, in *13th Symposium on Accelerator Physics* (2018)
- K. Abe, S. C. Joshi, T. Yamamura et al., GLC project: Linear collider for TeV physics (2003)
- T. Higo, Y. Higashi, S. Matsumoto et al., Advances in X-band TW Accelerator Structures Operating in the 100 MV/m Regime, in *Conf. Proc. C100523: THPEA013, 2010*, SLAC National Accelerator Lab., Menlo Park, CA (United States) (2012)
- A. Larsen, The Next Linear Collider Design: NLC 2001, SLAC National Accelerator Lab., Menlo Park, CA (United States) (2001)
- J. Wang, Accelerator structure development for NLC/GLC, Stanford Linear Accelerator Center, Menlo Park, CA (US) (2004)
- C. Adolphsen, Normal-conducting RF structure test facilities and results. Proceedings of the 2003 Particle Accelerator Conference, **1**, 668–672 (2003) <https://doi.org/10.1109/PAC.2003.1289005>
- T. Higo, M. Akemoto, A. Enomoto et al., High gradient study at KEK on X-band accelerator structure for linear collider. Proceedings of the 2005 Particle Accelerator Conference, 1162–1164 (2005). <https://doi.org/10.1109/PAC.2005.1590694>
- S. Döbert, Status and future prospects of CLIC. *Proceedings of LINAC08, Victoria, BC, Canada* (2009)
- J. Beijers, S. Brandenburg, K. Eikema et al., ZFEL: A Compact, Soft X-ray FEL in the Netherlands, in *Proceedings of FEL Malmö Sweden* (2010)
- Y. Sun, C. Adolphsen, C. Limborg-Deprey et al., Low-charge, hard X-ray free electron laser driven with an X-band injector and accelerator. Phys. Rev. ST Accel. Beams **15**, 030703 (2012). <https://doi.org/10.1103/PhysRevSTAB.15.030703>
- X. Huang, W. Fang, Q. Gu et al., Design of an X-band accelerating structure using a newly developed structural optimization procedure. Nucl. Instrum. Meth. A **854**, 45–52 (2017). <https://doi.org/10.1016/j.nima.2017.02.050>
- T. Lucas, Smart\*light, current activities and future concepts, in *International Workshop on Breakdown Science and High Gradient Technology* (2021)
- X. Wu, H. Zha, J. Shi et al., Design, fabrication, and high-gradient testing of X-band choke-mode damped structures. Phys. Rev. ST Accel. Beams **22**, 031001 (2019). <https://doi.org/10.1103/PhysRevAccelBeams.22.031001>
- M. Peng, J. Shi, H. Zha et al., Development and high-gradient test of a two-half accelerator structure. Nucl. Sci. Tech. **32**, 60 (2021). <https://doi.org/10.1007/s41365-021-00895-x>
- L. Zhou, H. Zha, J. Shi et al., Development of a high-gradient X-band RF gun with replaceable field emission cathodes for RF breakdown studies. Nucl. Instrum. Meth. A **1027**, 166206 (2022). <https://doi.org/10.1016/j.nima.2021.166206>
- J. Liu, J. Shi, A. Grudiev et al., Analytic RF design of a linear accelerator with a SLED-I type RF pulse compressor. Nucl. Sci. Tech. **31**, 107 (2020). <https://doi.org/10.1007/s41365-020-00815-5>
- Z. Farkas, H. Hoag, P. B. Wilson et al., SLED: A Method of Doubling SLAC's Energy, in *9th International Conference on High-Energy Accelerators* (1974).
- W. Fang, D. Tong, Q. Gu et al., Design and experimental study of a C-band traveling-wave accelerating structure. Chin. Sci. Bull. **56**, 18–23 (2011). <https://doi.org/10.1007/s11434-010-4265-2>
- T. Khabiboulline, V. Puntus, R. M. Dohlus et al., A new tuning method for traveling wave structures, in *Proceedings Particle Accelerator Conference*, 1666–1668 (1995). <https://doi.org/10.1109/PAC.1995.505321>
- R.H. Fowler, L. Nordheim, Electron emission in intense electric fields. **119**, 173–181 (1928). <https://doi.org/10.1098/rspa.1928.0091>
- J. Shi, A. Grudiev, W. Wuensch, Tuning of X-band traveling-wave accelerating structures. Nucl. Instrum. Meth. A **704**, 14–18 (2013). <https://doi.org/10.1016/j.nima.2012.11.182>
- C.W. Steele, A nonresonant perturbation theory. IEEE Trans. Microwave Theory Tech. **14**, 70–74 (1966). <https://doi.org/10.1109/TMTT.1966.1126168>
- W. Fan, A. Lu, L. L. Wai et al., Mixed-mode S-parameter characterisation of differential structures, in *Proceedings of the 5th Electronics Packaging Technology Conference (EPTC 2003)* (2003). <https://doi.org/10.1109/EPTC.2003.1271579>
- J. Shi, Dissertation, Tsinghua University, 2009 (in Chinese)
- X. Tao, D. Tong, A pass band performance simulation code of coupled cavities. in *22nd International Linear Accelerator Conference* (2004).
- P. Wang, J.-R. Shi, Z.-F. Xiong et al., Novel method to measure unloaded quality factor of resonant cavities at room temperature. Nucl. Sci. Tech. **29**, 50 (2018). <https://doi.org/10.1007/s41365-018-0383-3>

29. F. Liu, J. Shi, H. Zha et al., Development of a compact X-band variable-ratio RF power splitter. *Nucl. Instrum. Meth. A* **1015**, 165759 (2021). <https://doi.org/10.1016/j.nima.2021.165759>
30. X. Meng, J. Shi, H. Zha et al., Development of high-power S-band load. *Nucl. Instrum. Meth. A* **927**, 209–213 (2019). <https://doi.org/10.1016/j.nima.2019.02.002>
31. Y. Jiang, H. Zha, J. Shi et al., A compact X-band microwave pulse compressor using a corrugated cylindrical cavity. *IEEE Trans. Microwave Theory Tech.* **69**, 1586–1593 (2021). <https://doi.org/10.1109/TMTT.2021.3053913>
32. D. P. Pritzkau, Dissertation, Stanford University, 2001
33. W. Wuensch, A. Degiovanni, S. Calatroni et al., Statistics of vacuum breakdown in the high-gradient and low-rate regime. *Phys. Rev. ST Accel. Beams* **20**, 011007 (2017). <https://doi.org/10.1103/PhysRevAccelBeams.20.011007>

Springer Nature or its licensor holds exclusive rights to this article under a publishing agreement with the author(s) or other rightsholder(s); author self-archiving of the accepted manuscript version of this article is solely governed by the terms of such publishing agreement and applicable law.